X-ray nanodiffraction imaging reveals distinct nanoscopic dynamics of an ultrafast phase transition

Youngjun Ahn[a,b,1] 🄳, Mathew J. Cherukara[c] 🄳, Zhonghou Cai[a] 🄳, Michael Bartlein[c], Tao Zhou[c], Anthony DiChiara[a], Donald A. Walko[a], Martin Holt[c], Eric E. Fullerton[d], Paul G. Evans[b] 🄳, and Haidan Wen[a,e,2] 🄳

Ultrafast first-order phase transitions exhibit distinct transition pathways and dynamical properties that are not accessible during quasi-equilibrium transitions. Phenomena arising at the ultrafast timescale are important for understanding the transition mechanisms and in applications using the fast switching of electronic properties or magnetism. These transitions are accompanied by nanoscale structural dynamics that have been challenging to explore by optical or electronic transport probes. Here, X-ray nanodiffraction imaging shows that the nanoscale structural dynamics arising in ultrafast phase transitions differ dramatically from the transitions under slowly varying parameters. The solid-solid phase transitions in a FeRh thin film involve concurrent structural and magnetic changes and can be sensitively probed by monitoring their diffraction signatures following femtosecond optical excitation. Time-dependent nanodiffraction maps with 100-ps temporal and 25-nm spatial resolutions reveal that the preexisting nanoscale variation in phase composition results in spatially inhomogeneous changes of phase fraction after ultrafast optical excitation. The spatial inhomogeneity leads to nanoscale temperature variations and subsequent in-plane heat transport, which are responsible for spatially distinct relaxation pathways on nanometer length scales. The spatial gradients of the phase composition and elastic strain increase upon excitation rather than exhibiting the decrease previously reported in quasi-equilibrium transformations. Long-range elastic interactions thus do not play significant roles in the ultrafast phase transition. These microscopic insights into first-order phase transitions provide routes to manipulate nanoscopic phases in functional materials on ultrafast time scales by engineering initial nanoscale phase distributions.

nanoscopic imaging | structural dynamics | magnetic film | phase transition

First-order phase transitions are characterized by an abrupt change of an order parameter that parametrizes the degree of ordering in structural, electronic, or spin degrees of freedom. Ultrafast optical excitation of first-order phase transitions has the potential to allow high-speed manipulation of material properties for future technologies (1–5). A hallmark of first-order phase transitions is the coexistence of multiple phases (6–10), with phase heterogeneity at length scales as small as nanometers (10, 11). Although an extensive series of pump-probe studies have aimed to understand relevant ultrafast processes, the microscopic processes involved in ultrafast first-order phase transformations have just begun to be explored. Ultrafast nanoscopic imaging of phase transitions can reveal the dynamical evolution of the heterogeneity during the phase transition and the microscopic mechanism through which the ultrafast transitions occur.

Ultrafast nanoscale characterization methods based on optical (2, 12–15), electron (16, 17), and X-ray (18–23) microscopies have been recently developed and have revealed new physical phenomena. Hard X-ray microscopy is particularly advantageous in the study of phase transformations involving structural changes because X-ray diffraction is highly sensitive to structural heterogeneity, due to its high reciprocal-space resolution (24, 25). X-ray diffraction microscopy also preserves the spatially heterogenous stress state in complex structures such as quantum devices (25–27) because experiments do not require the preparation of the free-standing thin specimens typically required for transmission electron microscopy. Here, X-ray nanodiffraction microscopy combined with ultrafast optical excitation reveals that the nanoscale processes of the optically driven first-order phase transition in FeRh thin films are distinct from those occurring in a quasi-equilibrium transformation with slowly varying external parameters.

The intermetallic compound FeRh exhibits a first-order phase transition from a low-temperature antiferromagnetic (AFM) phase to a high-temperature ferromagnetic (FM) phase (28). Thin films of FeRh serve as an important platform to test concepts for

Significance

Phase transitions, the changes between states of matter with distinct electronic, magnetic, or structural properties, are at the center of condensed matter physics and underlie valuable technologies. First-order phase transitions are intrinsically heterogeneous. When driven by ultrashort excitation, nanoscale phase regions evolve rapidly, which has posed a significant experimental challenge to characterize. The newly developed laser-pumped X-ray nanodiffraction imaging technique reported here has simultaneous 100-ps temporal and 25-nm spatial resolutions. This approach reveals pathways of the nanoscale structural rearrangement upon ultrafast optical excitation, different from those transitions under slowly varying parameters. The spatiotemporally resolved structural characterization provides crucial nanoscopic insights into ultrafast phase transitions and opens opportunities for controlling nanoscale phases on ultrafast time scales.

[1]Present address: Department of Physics, University of Michigan, Ann Arbor, MI 48109.

[2]To whom correspondence may be addressed. Email: wen@anl.gov.

applications in magnetic data storage (29–31). The AFM-FM phase transition in FeRh and related materials has been intensively studied on the ultrafast time scale (3, 32–36) and the nanometer length scale (37–42), separately. Early optical pump-probe studies (3, 32) initially suggested that the onset of magnetic phase transitions occurs at subpicosecond time scales through the rapid nucleation of the FM phase. Recent time-resolved X-ray studies (33–36), however, show that simultaneous structural and magnetic transformation occurs on tens to hundreds of picosecond time scales. Static X-ray imaging studies of FeRh (37, 38, 40) show that phase heterogeneity is evident on nanometer scales and changes as a function of temperature. The separate use of spatially and temporally resolved probes, however, has not revealed the dynamics of nanoscale phase transformations in FeRh.

We have developed a laser-pumped synchrotron hard X-ray diffraction nanoprobe with spatiotemporal resolutions of 25 nm and 100 ps. This instrument integrated an ultrafast laser system into a hard X-ray nanoprobe beamline for pump-probe experiments. Spatiotemporal X-ray nanodiffraction maps revealed several key nanoscale processes of the first-order phase transition in FeRh. First, the optically induced transformation is highly influenced by the preexisting spatial distribution of the FM phase, resulting in a spatially heterogeneous phase transition. The relationship between the preexisting FM phase and the optically induced FM phase suggests a mechanism in which the growth of the preexisting FM domains contributes to the phase transition over the first 100 ps. Second, the relaxation dynamics are consistent with in-plane nanoscale heat transport. This in-plane heat transport is a consequence of the spatial variation of the temperature rise due to the preexisting FM phase. Third, the spatial gradients of both the nanoscale strain and the phase composition increase upon optical excitation, suggesting that the transient structural state after optical excitation has higher elastic energy than the initial state, in contrast to structural transformations as the temperature slowly varies.

Results

Characterization of FeRh Thin Films and Laser-Pumped Synchrotron Hard X-Ray Nanodiffraction.
FeRh has the CsCl crystal structure and exhibits AFM ordering with magnetic moments of ± 3 μ_B on the Fe atoms and zero magnetic moment on the Rh atoms below the AFM-FM transition temperature T_{AFM-FM} (28), as illustrated in Fig. 1A. At high temperatures, FeRh is in the FM phase with a magnetic moment of 1 μ_B on the Rh atoms, which are ferromagnetically coupled to nearest Fe neighbors (43). Our temperature-dependent X-ray diffraction measurements show that the epitaxial FeRh films exhibit a phase transition starting at 360 K with an out-of-plane lattice expansion (Fig. 1B) (see *Materials and Methods*). Fig. 1C displays a diffraction profile along the detector angle 2θ at 370 K. The profile shows a broadening of the X-ray reflection as a result of the coexistence of structurally distinct AFM and FM phases (*SI Appendix,* Fig. S1). The FM phase fraction within the probed volume can be obtained by using the two-peak fitting method (34) with the FM phase volume fraction given by $f_{FM} = I_{FM}/(I_{FM} + I_{AFM})$ where I_{FM} and I_{AFM} are the integrated diffraction intensities from FM phase and AFM phase, respectively. The investigated FeRh thin film shows a spatially homogeneous AFM phase at room temperature (*SI Appendix,* Fig. S2).

Laser-pumped synchrotron hard X-ray diffraction nanoprobe measurements were developed and conducted at the hard X-ray nanoprobe beamline of the Advanced Photon Source, as illustrated in Fig. 1D. X-ray pulses with a photon energy of 11 keV and 100 ps pulse duration were focused to a full-width-at-half-maximum (FWHM) spot size of 25 nm employing high-numerical-aperture X-ray focusing optics consisting of a Fresnel zone plate and an order-sorting aperture. The detector images from nanoscale regions were obtained by raster-scanning focused X-ray probe beams across a FeRh sample (see *Materials and Methods*). Laser pulses with a central wavelength of 515 nm and a pulse duration of 400 fs were electronically synchronized to the synchrotron X-ray pulses. A laser incident fluence of 0.12 mJ cm^{-2} was used to excite the FeRh film. The absorbed fluence is calculated to be 0.07 mJ cm^{-2} using optical parameters of FeRh and experiment geometry (*SI Appendix,* section I). The phase composition and structural parameters were determined by analyzing diffraction patterns of the 002 FeRh reflection in detector images along 2θ at each scanned position. The experiments yielded nanoscale maps of structural variations with out-of-plane lattice parameters as a function of time (gray color maps in Fig. 1D). Further details of experimental methods are provided in *Materials and Methods*.

Nanoscale Variation of the Dynamics of the Optically Driven AFM-FM Phase Transition.
Fig. 2 presents maps of the FM phase fraction f_{FM} for three different delay times: $t = -0.1$ ns, 0.1 ns, and 1.5 ns. Positive values of t correspond to the laser pump pulse preceding the X-ray probe pulse. The values of f_{FM} are obtained from the diffraction patterns following the method described above. The map at -0.1 ns shows that f_{FM} varies spatially from 0.25 to 1, which is a signature of the AFM/FM phase coexistence as expected at 370 K (*SI Appendix,* section II). The spatial variation of f_{FM} is continuous rather than discrete because the size of individual AFM and FM phase domains is on the order of ~50 nm (41), smaller than that of the effective X-ray probe size of 136×25 nm^2 under the experimental condition (see *Materials and Methods*). The spatial variation of f_{FM} at this temperature partially originates from location-dependent transition temperatures, which have been attributed to local structural variations (37, 40, 44, 45). Upon optical excitation, f_{FM} generally exhibits an increase at $t = 0.1$ ns. The magnitude of optically driven change in f_{FM} varies at different locations. Nearly half of the probed regions exhibit a saturation of f_{FM} at 1 while the other areas have f_{FM} less than 1. This partial AFM-FM phase transition at $t = 0.1$ ns is consistent with the expectation that results from an absorbed fluence that is less than the latent heat per unit area of 0.14 mJ cm^{-2} (46) for a 27 nm-thick FeRh thin film. Since the nucleation and growth in FeRh complete at ~0.1 ns (34), the spatial measurement of f_{FM} at $t = 0.1$ ns reveals the spatially dependent ultrafast phase transition as a result of nucleation and growth. The regions with $f_{FM} < 1$ at $t = 0.1$ ns undergo either no change or their f_{FM} values continue to increase, as evident in the X-ray diffraction map measured at $t = 1.5$ ns. Whereas the regions with $f_{FM} = 1$ at $t = 0.1$ ns exhibit a relaxation in f_{FM} at $t = 1.5$ ns. The results clearly show that both the phase transition as monitored at 0.1 ns and subsequent relaxation dynamics are spatially inhomogeneous, although the dynamics faster than the temporal resolution of 0.1 ns, such as the onset of phase transition, cannot be resolved in our experiments.

To explore the nanoscale variations of the phase transition and its dynamics, the local changes in f_{FM} and the associated phase transition dynamics up to 15 ns after optical excitation were measured by scanning the X-ray probe along the y axis at X = 0 nm in Fig. 2. The position-time map in Fig. 3A exhibits
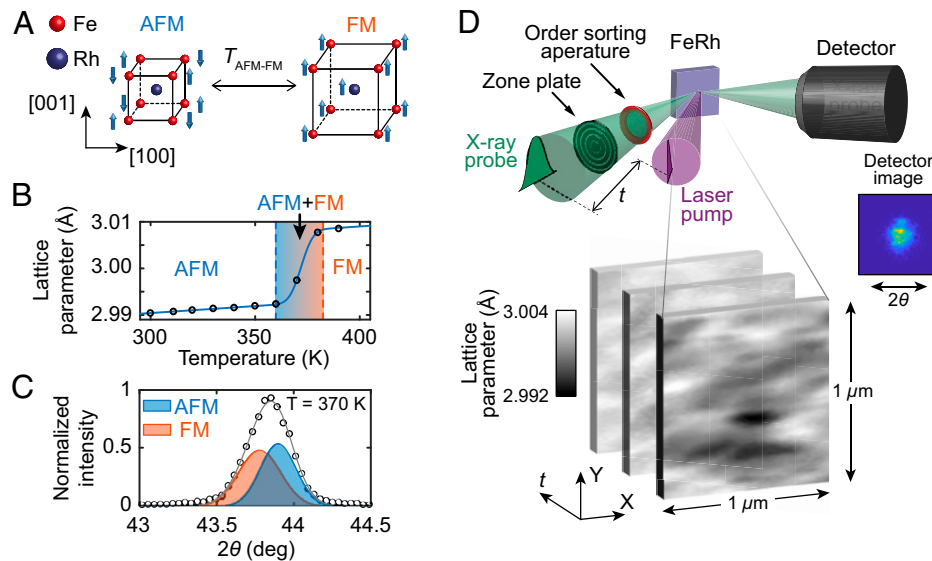
Fig. 1. Ultrafast X-ray nanoimaging of a first-order phase transition. (*A*) Illustration of the unit cells of AFM and FM phases in FeRh. The AFM-FM magnetic phase transition occurs at the transition temperature T_{AFM-FM} accompanied by a lattice expansion visualized exaggeratedly. Blue arrows indicate the directions of the magnetic moments of Fe and Rh atoms. (*B*) Out-of-plane lattice parameter as a function of temperature during heating. The shaded region indicates the temperature range in which AFM/FM phases coexist. (*C*) Diffraction profile of the 002 FeRh reflection along the detector angle 2θ at 370 K measured by a 50 μm X-ray beam. (*D*) Schematic of the optical pump, hard X-ray probe experiment at the 26-ID beamline of the Advanced Photon Source. Detector images are measured at each X-ray probe location by raster-scanning the X-ray beam across the sample. 1 × 1 μm² maps of lattice parameter at different t are extracted from the 2θ value of the 002 Bragg peak.

spatial variations of f_{FM} both before and after optical excitation. The subsequent change in f_{FM} following optical excitation also shows spatially dependent relaxation dynamics. The spatial dependence of the phase transition is examined by plotting the variation of the FM phase fraction $f_{FM}(0.1\ ns)$ after optical excitation as a function of the preexisting FM phase fraction $f_{FM}(-0.1\ ns)$, as shown in Fig. 3*B*. A key feature of spatially dependent phase transitions is evident in the relationship between $f_{FM}(0.1\ ns)$ and $f_{FM}(-0.1\ ns)$, exhibiting two distinct regimes of the AFM-FM phase transition: (i) for values of $f_{FM}(-0.1\ ns)$ less than 0.55, there is a monotonic increase in $f_{FM}(0.1\ ns)$ as a function of $f_{FM}(-0.1\ ns)$; and (ii) for values of $f_{FM}(-0.1\ ns)$ between 0.55 and 1, $f_{FM}(0.1\ ns)$ saturates at 1.

The monotonic trend as a function of $f_{FM}(-0.1\ ns)$ in regime (i) can be described by Avrami kinetics (47). The FM phase fraction at 0.1 ns is given by $f_{FM}(0.1\ ns) = f_{FM}(-0.1\ ns) + \Delta f_{FM}$, where Δf_{FM} is a transformed fraction of FM phase at $t = 0.1$ ns. Assuming a spatially random distribution of FM phase regions, the transformed FM fraction is $\Delta f_{FM}(t) = 1 - e^{-Kt^n}$, where K is the growth rate and n is the Avrami exponent. The phase transitions in thin films generally exhibit $n = 2$, indicating quasi-instantaneous heterogeneous nucleation followed by two-dimensional domain

growth (48, 49). The growth rate K is defined as $K = \pi\rho v^2$ for the phase transition with $n = 2$ where ρ is the density of FM nucleation per unit area and v is the growth velocity (47). The spatially dependent density of FM nucleation is defined by $\rho = \rho_{ave} f_{FM}(-0.1\ ns)$ where ρ_{ave} is the average nucleation density in the mapped area. Based on Fig. 2, we estimate the nucleation density ρ_{ave} to be $2 \times 10^{13}\ m^{-2}$ by counting the number of domains per unit area, which sets the lower bound of the nucleation density because each domain can grow from at least one nucleation. Using v as the only fitting parameter, the best fitting result (the blue curve in Fig. 3*B*) shows $v = 1.3 \times 10^3\ m\ s^{-1}$. This value represents the upper bound of the growth speed of FM domains in the probed region. The obtained value of the growth velocity is smaller than the longitudinal sound speed of $5.1 \times 10^3\ m\ s^{-1}$ in FeRh, which is consistent with the slower phase front propagation speed of the laser-induced phase transition than the speed of sound (19, 34). The dependence of the transformation on the number of preexisting FM nucleation provides an evidence that the growth contributes to the AFM-FM phase transition within 100 ps upon excitation, a process that was not captured by the previous ensemble-averaged experiments (34).
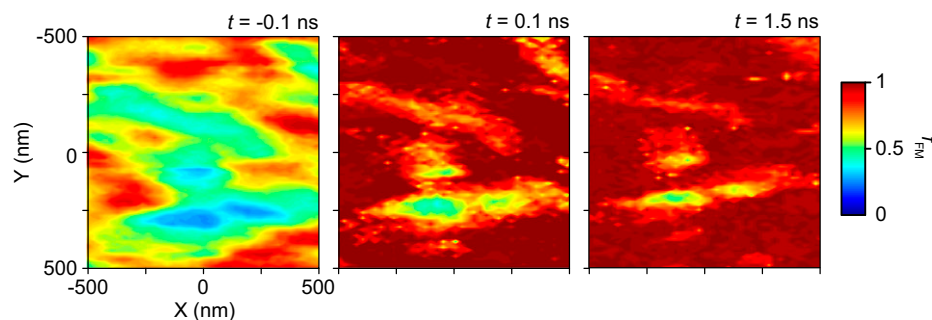
Fig. 2. X-ray nanodiffraction maps of the FM phase fraction f_{FM} at three delay times: $t = -0.1$ ns, 0.1 ns, and 1.5 ns. The image at $t = -0.1$ ns corresponds to the state at a steady-state temperature of 370 K.
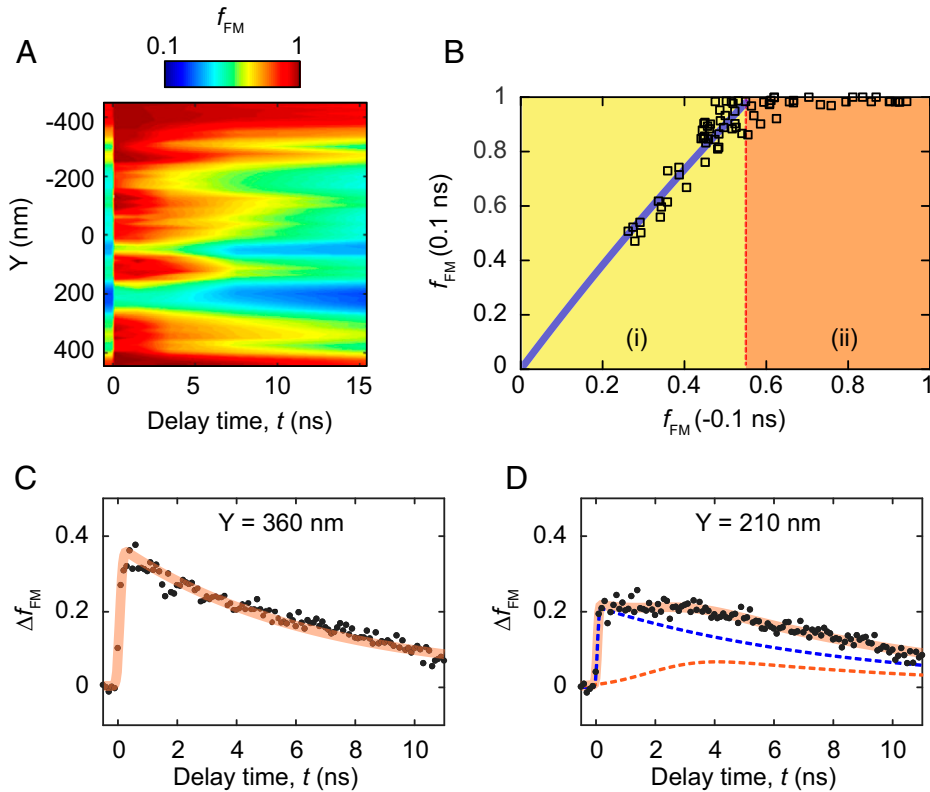
Fig. 3. Nanoscopic dynamics of phase composition. (*A*) Space- and time-resolved FM phase fraction f_{FM} measured along the *y* axis at X = 0 nm in Fig. 2. (*B*) FM phase fraction $f_{FM}(0.1$ ns) as a function of the initial FM phase fraction $f_{FM}(-0.1$ ns) obtained from the data shown in (*A*). Blue curve is a fit based on the Avrami equation (see text). (*C* and *D*) Changes (dots) in f_{FM} as a function of *t* measured at Y = 360 nm and Y = 210 nm at which the initial FM phase fraction is larger and less than 0.55, respectively. Solid and dashed curves are the fits by the phenomenological thermal-transport models described in the main text.

In regime (ii), the AFM phase is completely converted to the FM phase by optical excitation, as indicated by the saturation of $f_{FM}(0.1$ ns) at 1, because the absorbed energy is larger than the latent heat required to complete the phase transition. The excess energy, the difference between the absorbed energy and latent heat, further raises the temperature in these regions. Because the excess energy is larger in higher $f_{FM}(-0.1$ ns) regions, the temperature rises spatially vary, contributing to subsequent heat transport processes as discussed in detail below.

We next examine the nanoscale variation of the relaxation dynamics of Δf_{FM}. Fig. 3 *C* and *D* show Δf_{FM} as a function of delay time at two positions with coordinates Y = 360 nm and 210 nm, at which the values of $f_{FM}(-0.1$ ns) are larger and smaller than 0.55, respectively. The relaxation time scales at these two positions differ significantly, in particular, in the range from 0.1 ns to 3 ns. A phenomenological model can be used to quantify the time dependence of f_{FM} (*SI Appendix*, section III and Fig. S3). As shown in Fig. 3*C*, the relaxation of Δf_{FM} in the high $f_{FM}(-0.1$ ns) region exhibits a good agreement with a time-dependent phase fraction change $\Delta f_{FM} \sim \left[f_{rise}(t, t_1, \xi_1) e^{-\frac{t-t_1}{\tau_0}} \right]$. Here $f_{rise}(t, t_i, \xi_i) = \left(1 + \text{erf} \left(\frac{2\sqrt{2}(t-t_i)}{\xi_i} \right) \right)$ describes the increase in f_{FM}, modeled by an error-function with the rising edge at a time t_i and a time constant ξ_i. The factor $e^{-\frac{t-t_i}{\tau_0}}$ represents an exponential decay of the transformed fraction with a time constant τ_0 starting at t_i. This relaxation of the FM phase fraction is consistent with the cooling of the film through the heat transport from the film to the substrate, which can be approximated by an exponential decay within the relatively narrow time window of Fig. 3*C*. In

Fig. 3*D*, Δf_{FM} shows a transient plateau from 0.1 ns to 3 ns, in poor agreement with the exponential decay model, which indicates that additional processes occur at this location. To model these previously unknown processes, we have modified the model by adding a second term to the model for Δf_{FM} in regions of low $f_{FM}(-0.1$ ns): $\Delta f_{FM} \sim \left[f_{rise}(t, t_1, \xi_1) e^{-\frac{t-t_1}{\tau_0}} \right] + \left[f_{rise}(t, t_2, \xi_2) e^{-\frac{t-t_2}{\tau_0}} \right]$. The first term in the decay model describes a fast rise within 0.1 ns and the subsequent relaxation on the nanosecond time scale, shown by the blue dashed line in Fig. 3*D*, similar to the observation at Y = 360 nm. The second term describes a process that leads to an additional slow increase of the phase fraction up to 3.5 ns and relaxes on the same time scale (red dashed line in Fig. 3*D*). The combined result of the first and second terms in the model provides an excellent fit to the data. The contribution of the second term to the relaxation dynamics is consistently observed in regions with $f_{FM}(-0.1$ ns) < 0.55.

The spatial variations of the relaxation timescale are attributed to distinct heat-transport processes resulting from the nanoscale temperature variations upon optical excitation. In regions where $f_{FM}(-0.1$ ns) < 0.55, most of the absorbed optical energy is devoted to supplying the latent heat for the phase transition so that the sample temperature does not change significantly. In regions where $f_{FM}(-0.1$ ns) > 0.55, however, only a portion of the absorbed energy is used for the phase transition. The remaining energy leads to further temperature increases of the FM phase. The expected temperature rise due to the absorbed fluence is calculated by the equation $\Delta T = F_{abs}/(C_{FeRh} \times D)$ where F_{abs} is the absorbed fluence, C_{FeRh} is a specific heat of FeRh (33), and *D* is the thickness of the thin
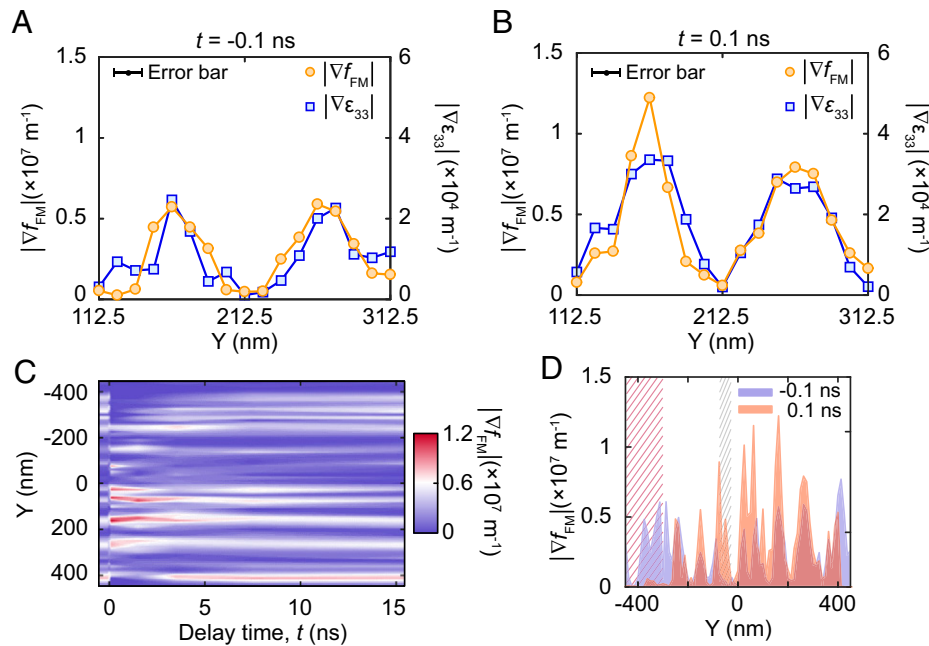
Fig. 4. Time-dependent phase composition gradient $|\nabla f_{FM}|$ and strain gradient $|\nabla \varepsilon_{33}|$. (*A* and *B*) Line profiles of $|\nabla f_{FM}|$ (circles) and $|\nabla \varepsilon_{33}|$ (squares) at $t =$ −0.1 ns and 0.1 ns. The data are obtained from Y = 112.5 nm to 312.5 nm in Fig. 3*A*. Error bar indicates the experimental uncertainty of ±10 nm. (*C*) Time-dependent $|\nabla f_{FM}|$ along the *y* axis in the region identical to Fig. 3*A*. (*D*) Spatial variation of $|\nabla f_{FM}|$ at $t =$ −0.1 (blue) and 0.1 ns (orange). The red and gray stripe patterns highlight the regions where the $|\nabla f_{FM}|$ peaks disappear and appear, respectively, after excitation.

film. The absorbed fluence of 0.07 mJ cm^{-2} can lead to a maximum temperature change of the FM phase by 5.6 K. Thus, the in-plane temperature gradient from high $f_{FM}(-0.1$ ns) to low $f_{FM}(-0.1$ ns) regions emerges upon optical excitation. As a result, the in-plane heat diffusion leads to a slow secondary increase in the FM phase fraction in the low $f_{FM}(-0.1$ ns) region, which is well described by the second component in the phenomenological model. The slow rate of the phase transition in low-$f_{FM}(-0.1$ ns) regions is apparent in the map collected at $t = 1.5$ ns (Fig. 2). The characteristic in-plane heat diffusion time is $\xi_{char} \sim L^2/\alpha$, where L is a distance between two probed regions and α is the thermal diffusivity. With $\alpha = 0.9 \times 10^{-5}$ m^2/s (50, 51) and $L = 150$ nm, we obtain $\xi_{char} \sim 2.5$ ns, which agrees with the observed characteristic time scale of $\xi_2 = 3.2 \pm 1.6$ ns (*SI Appendix*, section III).

Nanoscale Phase Composition and Microstructure during the Phase Transition. The spatial variation of the FM phase composition and the structural distortion during the phase transition can be extracted by measuring the magnitude of the spatial gradient of f_{FM} and out-of-plane strain ε_{33}, termed $|\nabla f_{FM}|$ and $|\nabla \varepsilon_{33}|$, respectively. Fig. 4*A* displays line profiles of $|\nabla f_{FM}|$ and $|\nabla \varepsilon_{33}|$ at $t = -0.1$ ns from Y = 112.5 nm to 312.5 nm in Fig. 3*A*. Local maxima in both $|\nabla f_{FM}|$ and $|\nabla \varepsilon_{33}|$ are observed at Y = 160 nm and 260 nm, indicating the significant spatial variation of both phase composition and strain at these locations. The observed strain gradient of 10^4 m^{-1} is consistent with the strain gradient sustainable in thin films (52). Upon optical excitation, $|\nabla f_{FM}|$ and $|\nabla \varepsilon_{33}|$ increase while the locations of the maxima of $|\nabla f_{FM}|$ and $|\nabla \varepsilon_{33}|$ do not shift within the experimental uncertainty of ±10 nm as shown in Fig. 4*B*.

The observations above are distinct from what was found when the phase transition is driven by slowly varying the temperature (37). In that case, nanoscale strain fields and the accompanying distribution of phases gradually shift and

disappear during the structural phase transition. The spatial variations of the phase composition and strain are the consequences of the competing short- and long-range interactions (10, 11, 53). When the temperature slowly varies, long-range elastic interactions minimize the free energy through the reduction of the elastic strain energy (53). However, the observation of larger gradients of both f_{FM} and ε_{33} indicates that the elastic energy increases upon excitation, in contrast to the elastic energy relaxation observed when the order parameters slowly vary. These results suggest that the long-range elastic interaction does not significantly contribute to the free energy landscape during the ultrafast phase transition in this system, consistent with the sharpening of domain walls observed during an ultrafast structural phase transition in a 1*T*-TaS$_2$ crystal (17).

Fig. 4*C* shows a position-time map of $|\nabla f_{FM}|$ spanning 0.9 μm in length. Comparing with Fig. 4 *A* and *B*, this wider range shows various characteristic responses that are present across the sample. Most locations generally undergo increases in $|\nabla f_{FM}|$ upon excitation as discussed in Fig. 4 *A* and *B*, while the changes in $|\nabla f_{FM}|$ relax fully within 15 ns. The positions of most $|\nabla f_{FM}|$ maxima do not exhibit a transient shift within the probed delay time. Fig. 4*D* compares the phase composition gradient $|\nabla f_{FM}|$ in the same wide range before and after the excitation at $t = 0.1$ ns. The regions from Y = −300 nm to −450 nm, indicated by the red striped pattern, display a reduction of $|\nabla f_{FM}|$, distinct from the general change in $|\nabla f_{FM}|$. This decrease in $|\nabla f_{FM}|$ results from the reduced phase heterogeneity followed by the completion of the AFM-FM phase transition, i.e., $f_{FM}(0.1$ ns) = 1, at the positions where $f_{FM}(-0.1$ ns) is larger than 0.55 as presented in Fig. 3*A*. In rare cases (e.g., around Y = −50 nm shaded by gray-striped pattern), we also note that a new maximum of $|\nabla f_{FM}|$ appears upon photoexcitation, which may be caused by intrinsic structural defects that alter the photoinduced structural changes locally.

Discussion

The behavior of FeRh at the AFM-FM transition temperature is relevant to the operating conditions of heat-assisted magnetic recording (29). The phase-transition dynamics as observed close to the transition temperature provide several important perspectives for the potential applications. First, the strong dependence of the phase transition on the FM phase fraction implies a possible strategy to control the magnitude and dynamics of the nanoscale phase transition by varying preexisting FM phase composition. Second, a narrow region with phase gradient between heterogeneous phases can be realized on ultrafast time scales, rather than broadened phase gradient which typically forms through long-range elastic interactions under quasi-equilibrium conditions (53). This observation indicates that nanometer magnetic domains with sharper boundaries can be achieved by ultrafast excitation. Third, the structural nanoscale phase transition processes are reversible at subnanosecond time-scale as presented in this study because the same pathway occurs over thousands of pump-probe cycles during the measurements. This phenomenon may originate in a structural pinning effect that has also been observed during the slow thermal cycling (37). This reversible rather than irreversible process is particularly important for manipulating phases in a predictable manner for magnetic recording accompanied by structural phase transitions on the ultrafast timescale. We note that the irreversible process may present during ultrafast phase transition, but the pump-probe technique used in this study is not sensitive to them.

In conclusion, the laser-pumped synchrotron hard X-ray nanodiffraction technique enables the nanoscale visualization of physical phenomena during the optically driven first-order structural phase transitions. Our observations reveal a strong dependence of the AFM-FM phase transition of FeRh on preexisting FM domains after optical excitation. The spatially inhomogeneous relaxation dynamics is a consequence of spatially varying phase transformation leading to an additional in-plane thermal transport. We further find that the phase transition driven by ultrafast energy deposition results in an increase in the strain gradient, distinct from the case under slowly varying temperature conditions. It suggests that the effect of the long-range elastic interaction in the structural phase transition can be different depending on the rate of energy deposition, providing a nanoscopic perspective of phase transition dynamics. Besides studying nanoscale phase transitions, the spatiotemporally resolved X-ray diffraction demonstrated here can be applied to a wide range of functional materials and devices for studying nanoscale dynamical phenomena that are previously inaccessible.

Materials and Methods

Sample Preparation. An epitaxial FeRh thin film with a thickness of 27 nm was deposited on a (001)-oriented MgO substrate by the comagnetron sputtering method. Due to the lattice mismatch between the film and the substrate, the in-plane compressive strain was applied to the FeRh thin film, resulting in tetragonally distorted FeRh film. The transition temperature of FeRh film is $T_{AFM-FM} = 360$ K, above which AFM phases start to transform into FM phase spanning a temperature range of ~20 K. The magnetic phase transition is accompanied by a structural distortion along the out-of-plane direction.

Laser-Pumped Synchrotron Hard X-Ray Diffraction Nanoprobe Technique. The laser-pumped synchrotron hard X-ray diffraction nanoprobe technique was implemented at the 26-ID-C beamline of the Advanced Photon Source (APS)

at Argonne National Laboratory. Laser pulses with a central wavelength of 515 nm were provided by the second harmonic generation from the fundamental wavelength of 1,030 nm from a high-repetition-rate laser (Satsuma, Amplitude Laser). The laser repetition rate was tuned to 271 kHz to match the repetition rate of the singlet X-ray pulse in the hybrid fill operation mode of the APS. The sample, X-ray optics, and optomechanical nanopositioning system were housed in a vacuum chamber. The laser pulse, with a maximum energy of 3.5 μJ, was focused by a pair of concave and convex lenses. The distance between the two lenses was adjusted to vary the laser spot size. The focused beam entered the vacuum chamber through a viewport and propagated about 70 cm to the sample surface. The smallest spot size at the sample surface (full-width-at-half-maximum) was 0.4 mm. The laser incident angle was 25° with respect to the sample surface. The maximum incident fluence was 0.12 mJ cm^{-2}. X-ray pulses with a photon energy of 11 keV and 100 ps pulse duration were focused on the sample surface with an incident angle of 22.16° with respect to the sample surface, satisfying the Bragg condition of the 002 FeRh reflection. Due to the X-ray footprint, the X-ray spot size was elongated along the horizontal direction. The spot size on the sample surfaces was 25 nm (vertical) × 70 nm (horizontal) while the smallest resolvable feature size, in consideration of the sample thickness and diffraction geometry, is 136 nm (*SI Appendix*, Fig. S4). Thus, the effective spot size is 136 × 25 nm^2. A two-dimensional pixel array detector was positioned at 23.9 cm from the focused X-ray spot on the sample and gated to capture the X-ray diffraction pattern at a given delay time. Location-dependent X-ray diffraction patterns were measured by scanning the X-ray beam via X-ray focusing optics across the sample in the transverse plane with respect to the X-ray propagation direction with a step size ranging from 10 nm to 30 nm. The scales of the X-axis in the resultant real-space maps have been corrected by considering the crossing angle of 67.84° between the X-ray scanning axis and the sample X-axis shown in Fig. 2.

The lattice parameters of FeRh were measured without scanning the X-ray incident angle in our experiment. A Fresnel zone plate was used to focus the X-ray pulse with an angular divergence of $\Delta\theta = 0.48°$ at a photon energy of 11 keV. Due to the large divergence of the focused X-ray beam, the geometry at a fixed incident angle satisfied the Bragg condition in a range of $\Delta\theta$. Based on the diffraction geometry, this angular range corresponded to 2% of lattice parameter changes in FeRh. This change was larger than the expected change in the lattice parameter (0.6%) during the structural phase transition in FeRh. It was thus sufficient to obtain the 2θ value of the peak using the centroid of the diffraction patterns at the fixed incident angle on the pixel array detector during the phase transition.

Temperature-Dependent X-Ray Diffraction. X-ray diffraction measurements at a series of temperatures were conducted at station 7-ID-C of the APS. The photon energy and the spot size of the X-ray beam were 11 keV and 50 μm, respectively. The FeRh film on the MgO substrate was placed on a heating stage mounted on a six-circle Huber diffractometer. The temperature of the heating stage was electronically controlled (Lakeshore model 340). Diffracted X-rays were measured by a two-dimensional pixel array detector (Pilatus 100 K) placed 99.5 cm from the FeRh sample. The 002 FeRh reflection was measured as a function of temperature ranging from 300 K to 390 K with a step size of 10 K. The lattice parameters along the out-of-plane direction were obtained by measuring the θ-2θ curve of 002 FeRh reflection.

Madison, WI 53706; [c]Center for Nanoscale Materials, Argonne National Laboratory, Lemont, IL 60439; [d]Center for Magnetic Recording Research, University of California San Diego, La Jolla, CA 92903; and [e]Materials Science Division, Argonne National Laboratory, Lemont, IL 60439

Author affiliations: [a]Advanced Photon Source, Argonne National Laboratory, Lemont, IL 60439; [b]Department of Materials Science and Engineering, University of Wisconsin–Madison,

1. Z. Yang, C. Ko, S. Ramanathan, Oxide electronics utilizing ultrafast metal-insulator transitions. *Annu. Rev. Mater. Res.* **41**, 337–367 (2011).
2. M. Eisele *et al.*, Ultrafast multi-terahertz nano-spectroscopy with sub-cycle temporal resolution. *Nat. Photonics* **8**, 841–845 (2014).
3. G. Ju *et al.*, Ultrafast generation of ferromagnetic order via a laser-induced phase transformation in FeRh thin films. *Phys. Rev. Lett.* **93**, 197403 (2004).
4. Z. Chen, J.-W. Luo, L.-W. Wang, Revealing angular momentum transfer channels and timescales in the ultrafast demagnetization process of ferromagnetic semiconductors. *Proc. Natl. Acad. Sci. U.S.A.* **116**, 19258–19263 (2019).
5. M. R. Otto *et al.*, How optical excitation controls the structure and properties of vanadium dioxide. *Proc. Natl. Acad. Sci. U.S.A.* **116**, 450–455 (2019).
6. K. Binder, Theory of first-order phase transitions. *Rep. Prog. Phys.* **50**, 783–859 (1987).
7. M. Uehara, S. Mori, C. H. Chen, S.-W. Cheong, Percolative phase separation underlies colossal magnetoresistance in mixed-valent manganites. *Nature* **399**, 560–563 (1999).
8. H. T. Stinson *et al.*, Imaging the nanoscale phase separation in vanadium dioxide thin films at terahertz frequencies. *Nat. Commun.* **9**, 3604 (2018).
9. R.-Y. Dong, S. Granick, Reincarnations of the phase separation problem. *Nat. Commun.* **12**, 911 (2021).
10. A. S. McLeod *et al.*, Nanotextured phase coexistence in the correlated insulator V_2O_3. *Nat. Phys.* **13**, 80–86 (2017).
11. M. Seul, D. Andelman, Domain shapes and patterns: The phenomenology of modulated phases. *Science* **267**, 476–483 (1995).
12. S. A. Dönges *et al.*, Ultrafast nanoimaging of the photoinduced phase transition dynamics in VO_2. *Nano Lett.* **16**, 3029–3035 (2016).
13. M. Wagner *et al.*, Ultrafast and nanoscale plasmonic phenomena in exfoliated graphene revealed by infrared pump-probe nanoscopy. *Nano Lett.* **14**, 894–900 (2014).
14. J. Del Valle *et al.*, Spatiotemporal characterization of the field-induced insulator-to-metal transition. *Science* **373**, 907–911 (2021).
15. M. A. Huber *et al.*, Ultrafast mid-infrared nanoscopy of strained vanadium dioxide nanobeams. *Nano Lett.* **16**, 1421–1427 (2016).
16. D. R. Cremons, D. A. Plemmons, D. J. Flannigan, Femtosecond electron imaging of defect-modulated phonon dynamics. *Nat. Commun.* **7**, 11230 (2016).
17. T. Danz, T. Domröse, C. Ropers, Ultrafast nanoimaging of the order parameter in a structural phase transition. *Science* **371**, 371–374 (2021).
18. H. Wen, M. J. Cherukara, M. V. Holt, Time-resolved X-ray microscopy for materials science. *Annu. Rev. Mater. Res.* **49**, 389–415 (2019).
19. Y. Zhu *et al.*, Mesoscopic structural phase progression in photo-excited VO_2 revealed by time-resolved x-ray diffraction microscopy. *Sci. Rep.* **6**, 21999 (2016).
20. R. M. Karl Jr. *et al.*, Full-field imaging of thermal and acoustic dynamics in an individual nanostructure using tabletop high harmonic beams. *Sci. Adv.* **4**, eaau4295 (2018).
21. S. J. Whiteley, F. J. Heremans, G. Wolfowicz, D. D. Awschalom, M. V. Holt, Correlating dynamic strain and photoluminescence of solid-state defects with stroboscopic x-ray diffraction microscopy. *Nat. Commun.* **10**, 3386 (2019).
22. Y. Ahn *et al.*, Nanosecond optically induced phase transformation in compressively strained $BiFeO_3$ on $LaAlO_3$. *Phys. Rev. Lett.* **123**, 045703 (2019).
23. T. D. Frazer *et al.*, Optical transient grating pumped X-ray diffraction microscopy for studying mesoscale structural dynamics. *Sci. Rep.* **11**, 19322 (2021).
24. M. Holt, R. Harder, R. Winarski, V. Rose, Nanoscale hard X-ray microscopy methods for materials studies. *Annu. Rev. Mater. Res.* **43**, 183–211 (2013).
25. P. G. Evans *et al.*, Resonant nanodiffraction x-ray imaging reveals role of magnetic domains in complex oxide spin caloritronics. *Sci. Adv.* **6**, eaba9351 (2020).
26. J. Park *et al.*, Electrode-stress-induced nanoscale disorder in Si quantum electronic devices. *APL Mater.* **4**, 066102 (2016).
27. A. Pateras *et al.*, Mesoscopic elastic distortions in GaAs quantum dot heterostructures. *Nano Lett.* **18**, 2780–2786 (2018).
28. V. L. Moruzzi, P. M. Marcus, Antiferromagnetic-ferromagnetic transition in FeRh. *Phys. Rev. B Condens. Matter* **46**, 2864–2873 (1992).
29. J.-U. Thiele, S. Maat, E. E. Fullerton, FeRh/FePt exchange spring films for thermally assisted magnetic recording media. *Appl. Phys. Lett.* **82**, 2859–2861 (2003).
30. X. Marti *et al.*, Room-temperature antiferromagnetic memory resistor. *Nat. Mater.* **13**, 367–374 (2014).
31. R. O. Cherifi *et al.*, Electric-field control of magnetic order above room temperature. *Nat. Mater.* **13**, 345–351 (2014).
32. J.-U. Thiele, M. Buess, C. H. Back, Spin dynamics of the antiferromagnetic-to-ferromagnetic phase transition in FeRh on a sub-picosecond time scale. *Appl. Phys. Lett.* **85**, 2857–2859 (2004).
33. F. Quirin *et al.*, Structural dynamics in FeRh during a laser-induced metamagnetic phase transition. *Phys. Rev. B* **85**, 020103 (2012).
34. S. O. Mariager *et al.*, Structural and magnetic dynamics of a laser induced phase transition in FeRh. *Phys. Rev. Lett.* **108**, 087201 (2012).
35. I. Radu *et al.*, Laser-induced generation and quenching of magnetization on FeRh studied with time-resolved x-ray magnetic circular dichroism. *Phys. Rev. B* **81**, 104415 (2010).
36. F. Pressacco *et al.*, Laser induced phase transition in epitaxial FeRh layers studied by pump-probe valence band photoemission. *Struct. Dyn.* **5**, 034501 (2018).
37. D. J. Keavney *et al.*, Phase coexistence and kinetic arrest in the magnetostructural transition of the ordered alloy FeRh. *Sci. Rep.* **8**, 1778 (2018).
38. S. O. Mariager, L. L. Guyader, M. Buzzi, G. Ingold, C. Quitmann, Imaging the antiferromagnetic to ferromagnetic first order phase transition of FeRh. *arXiv* [Preprint] (2013). https://arxiv.org/abs/1301.4164 (Accessed 7 January 2014).
39. J. L. Warren, C. W. Barton, C. Bull, T. Thomson, Topography dependence of the metamagnetic phase transition in FeRh thin films. *Sci. Rep.* **10**, 4030 (2020).
40. C. Baldasseroni *et al.*, Temperature-driven nucleation of ferromagnetic domains in FeRh thin films. *Appl. Phys. Lett.* **100**, 262401 (2012).
41. T. P. Almeida *et al.*, Direct visualization of the magnetostructural phase transition in nanoscale FeRh thin films using differential phase contrast imaging. *Phys. Rev. Mater.* **4**, 034410 (2020).
42. A. B. Mei *et al.*, Local photothermal control of phase transitions for on-demand room-temperature rewritable magnetic patterning. *Adv. Mater.* **32**, e2001080 (2020).
43. P. M. Derlet, Landau-Heisenberg Hamiltonian model for FeRh. *Phys. Rev. B Condens. Matter Mater. Phys.* **85**, 174431 (2012).
44. D. Wang, Y. Wang, Z. Zhang, X. Ren, Modeling abnormal strain states in ferroelastic systems: The role of point defects. *Phys. Rev. Lett.* **105**, 205702 (2010).
45. R. Fan *et al.*, Ferromagnetism at the interfaces of antiferromagnetic FeRh epilayers. *Phys. Rev. B Condens. Matter Mater. Phys.* **82**, 184418 (2010).
46. S. Maat, J.-U. Thiele, E. E. Fullerton, Temperature and field hysteresis of the antiferromagnetic-to-ferromagnetic phase transition in epitaxial FeRh films. *Phys. Rev. B* **72**, 214432 (2005).
47. M. Avrami, Kinetics of phase change. II transformation-time relations for random distribution of nuclei. *J. Chem. Phys.* **8**, 212–224 (1940).
48. H. S. Choi, J. S. Ahn, J. H. Jung, T. W. Noh, D. H. Kim, Mid-infrared properties of a VO_2 film near the metal-insulator transition. *Phys. Rev. B Condens. Matter* **54**, 4621–4628 (1996).
49. E. Abreu *et al.*, Dynamic conductivity scaling in photoexcited V_2O_3 thin films. *Phys. Rev. B Condens. Matter Mater. Phys.* **92**, 085130 (2015).
50. P. Tu, A. J. Heeger, J. S. Kouvel, J. B. Comly, Mechanism for the first-order magnetic transition in the FeRh system. *J. Appl. Phys.* **40**, 1368–1369 (1969).
51. M. J. Jiménez, A. B. Schvval, G. F. Cabeza, Ab initio study of FeRh alloy properties. *Comput. Mater. Sci.* **172**, 109385 (2020).
52. D. Lee *et al.*, Giant flexoelectric effect in ferroelectric epitaxial thin films. *Phys. Rev. Lett.* **107**, 057602 (2011).
53. N. Moelans, B. Blanpain, P. Wollants, An introduction to phase-field modeling of microstructure evolution. *Calphad* **32**, 268–294 (2008).